Finite-size effects on heat and mass transfer in porous electrodes

Citation for the original published paper (version of record):
Astaneh, M., Maggiolo, D., Ström, H. (2022). Finite-size effects on heat and mass transfer in porous electrodes. International Journal of Thermal Sciences, 179.
http://dx.doi.org/10.1016/j.ijthermalsci.2022.107610

International Journal of Thermal Sciences 179 (2022) 107610

Contents lists available at ScienceDirect

International Journal of Thermal Sciences

journal homepage: www.elsevier.com/locate/ijts

Finite-size effects on heat and mass transfer in porous electrodes

Majid Astaneh [a,b,*], Dario Maggiolo [a], Henrik Ström [a]

[a] Division of Fluid Dynamics, Department of Mechanics and Maritime Sciences, Chalmers University of Technology, 412 96 Göteborg, Sweden
[b] Northvolt AB, Alströmergatan 20, 112 47 Stockholm, Sweden

ARTICLE INFO

Keywords:
Finite-size effects
Porous electrodes
Heat transfer
Mass transfer
Lithium-ion battery

ABSTRACT

In thin electrode applications, as the ratio of the obstacle size with respect to the system size increases, issues such as finite-size effects become more influential in the transport of heat and mass within a porous structure. This study presents a numerical approach to evaluate the finite-size effects on the heat and mass transfer in porous electrodes. In particular, numerical simulations based on the lattice Boltzmann method (LBM) are employed to analyze the pore-scale transport phenomena. Analyzing the results at both the electrode level and the pore level shows that the mass transfer performance is more influenced by the finite-size effects compared to the transfer of heat. The numerical simulations show that as the parameter m being the ratio of the electrode thickness to the particle diameter is halved, the effective diffusivity increases by 20% while the effective conductivity remains unchanged. We propose a novel analytical tortuosity–porosity ($\tau-\phi$) correlation as $\tau = [1-(1-\phi)^{m+1}]/\phi$ where the finite-size effects are taken into account via the parameter m. Besides, particles of small size provide more uniform distributions of temperature and concentration within the porous structure with standard deviations of approximately half of the values obtained from the case made up of large particles. Our findings at the electrode level are compared with the commonly used macroscopic porosity-dependent correlations found in the literature. At the end, by performing a systematic assessment, we provide guidelines for efficient design of porous electrodes.

1. Introduction

The development of porous electrodes plays an indispensable role in the future design of electrochemical systems with high energy density and improved thermal performance [1]. Microstructural analysis and geometrical design of random porous media are of paramount importance in efficient descriptions of transport phenomena in a wide variety of engineering applications [2–5]. Xue et al. [6], by considering Lithium-ion (Li-ion) battery cell as a case study, highlighted the long-standing challenge of electrode design to fully utilize the potential of the active materials occupying porous electrodes.

Under Li-ion battery operation, the Li ions shuttle back and forth between the negative and positive electrodes. This leads to the occurrence of the kinetic and mass transport overpotentials and accordingly the cell resistance rises [7]. Consequently, the cell temperature increases as a result of the irreversible heat generation [8]. The performance of Li-ion batteries is greatly influenced by the heat transfer and the transport of ions within the electrode compartment. Temperature is a key factor affecting the long-term performance and safe operation of Li-ion batteries [9], while the rate performance of Li-ion batteries is limited by the ion transport efficiency at the electrode level [10].

Multiphysics simulation of electrochemical systems has faced an ever-increasing popularity in recent years [11,12]. The so-called macro-homogeneous electrochemical models link the effective transport-related parameters of the porous electrodes to the electrochemical cell and system performance [13]. Therefore, it is crucial to precisely and robustly correlate the electrode design factors (e.g. thickness, porosity and particle size) to the afore-stated parameters.

Progelhof et al. [14] provided a review on different approaches to obtain the effective thermal conductivity of composite materials. Among different methods, analytical and combinatory approaches have been commonly used for simple geometries due to their computational efficiency, appropriate accuracy and physical basis [3,15]. Volume-averaging is another commonly used method to estimate the effective thermal properties of electrochemical devices [16,17]. This approach, however, considers a mathematical homogenization of different phases constituting porous electrodes and thus may often be difficult to apply in practice. To tackle this problem, hybrid approaches have been

* Corresponding author at: Division of Fluid Dynamics, Department of Mechanics and Maritime Sciences, Chalmers University of Technology, 412 96 Göteborg, Sweden.
E-mail addresses: majid.astaneh@chalmers.se, majid.astaneh@northvolt.com (M. Astaneh), maggiolo@chalmers.se (D. Maggiolo), henrik.strom@chalmers.se (H. Ström).

https://doi.org/10.1016/j.ijthermalsci.2022.107610
Received 23 February 2022; Received in revised form 29 March 2022; Accepted 30 March 2022
Available online 20 April 2022

proposed where numerical and experimental methods are employed in predicting the effective thermal conductivity of a porous material [18]. For instance, Werner et al. [19] proposed a bottom-up framework by combining modeling and experimental approaches to reliably extract thermal conductivities of Li-ion cells and their electrode configurations. Wei et al. [20] recently developed an advanced machine learning-based method for fast estimation of effective thermal conductivities of the composite materials and the porous media. The authors found that the models obtained from their approach led to higher prediction accuracy compared to the conventionally used Maxwell–Eucken and Bruggeman models.

In the context of mass transfer in porous media, it has been shown that the presence of solid obstacles lead to the deviation of the component diffusion paths from straight lines [21,22]. Shen et al. [21] provided a critical review on the effect of tortuosity on diffusion where different analytical and empirical tortuosity–porosity relations were presented and compared to the measured data. It was observed that although the theoretical relations did not match the measurements accurately, the empirical approaches contained some tunable parameters and therefore were able to describe the experiments more appropriately. Among existing approaches, the original version of Bruggeman's equation [23], has been widely used in fuel cell and battery research to correlate the tortuosity factor of the porous media to the porosity as [8,24,25]:

$$D_{eff} = \frac{D_f \phi}{\tau}, \tag{1}$$

$$\tau = \phi^{1-\alpha}, \tag{2}$$

where D_{eff} and D_f are the effective and intrinsic diffusion coefficients respectively, ϕ is the porosity, τ is the tortuosity and α is the Bruggeman exponent. The Bruggeman correleation with $\alpha = 1.5$ is typically used in physics-based modeling of batteries and fuel cells [26–28]. However, Thorat et al. [29], by performing experimental tests on the porous Li-ion battery electrodes, realized that the oft-used version of the Bruggeman correlation led to the underestimation of mass transport resistance and therefore an empirical relation between porosity and tortuosity was proposed in their work. It was observed that the tortuosity of twice the value estimated by the Bruggeman relation was required to lead to a good agreement between the model and experiments concerning the relaxation decay rate. Xu et al. [13] correlated the Bruggeman exponent to the electrode's thickness for Li-ion batteries. Together with experimental validation, the authors concluded that the inclusion of the modified Bruggeman correlation into macro-homogeneous electrochemical models resulted in significant improvement in model predictability and accuracy. It was shown that for a typical NCM electrode with 130 μm thickness, by performing such a modification, around 35% improvement in the prediction of the cell deliverable capacity was achieved under 5 C discharge current.

Direct numerical simulations have been performed in porous media either to assess pore-scale transport phenomena [8,30] or to extract effective transport parameters to be fed into macro-homogeneous models [31,32]. Vadakkepatt et al. [31] mentioned that the commonly used version of Bruggeman's model fails to efficiently link the effective thermal conductivity of porous electrodes to the microstructure topology. By performing numerical investigations using a finite-volume scheme, the authors found that for a typical NCM cathode, the original value of the Bruggeman exponent needed recalibration (from $\alpha = 1.5$ up to α=2.5) to provide reliable outcomes. Goldin et al. [32] developed a three-dimensional (3D) particle-resolved model using finite-volume discretization scheme for Li-ion batteries to re-evaluate the empirical exponents used in one-dimensional models. In Refs. [33–35] authors employed numerical simulations to evaluate the effect of design parameters on the heat transfer performance and temperature uniformity for other engineering applications such as phase change materials.

Analyzing transport phenomena in complex geometries brings forth the development of efficient numerical techniques. Among existing tools, the lattice Boltzmann method (LBM) is a promising numerical scheme in both heat and mass transfer studies in different multiphase flow systems due to its ease of formulation and computational efficiency [36–39]. The LBM has been widely used in investigating transport processes in electrochemical systems since it provides additional detailed information that is not possible to extract easily from empirical/analytical correlations or experiments. For instance, Chen et al. [40] coupled finite-volume and lattice Boltzmann methods to develop a computationally efficient multi-scale framework to capture pore-scale transport phenomena in gas diffusion and catalyst layers of proton exchange membrane fuel cells. Qiu et al. [41] took advantage of the LBM to model the electrolyte flow in pore space for the case study of vanadium redox flow batteries. By solving for potential, concentration and current density distributions, the authors developed the so-called structure–property–performance framework for flow battery electrodes. Maggiolo et al. [38] presented a pore-scale numerical method based on LBM to simulate the reaction and solute transport in porous electrodes in the case of redox flow batteries. The LBM has also attracted popularity in microscopic investigation of Li-ion battery cells. Jiang et al. [42] studied ion and electron transport in porous Li-ion electrodes using LBM. It was shown that smaller cathode particle size and high cathode porosity together with larger anode particle size and low anode porosity led to improved battery performance. The application of lattice Boltzmann (LB) simulations in analyzing the impact of randomness in active material particle distribution and particle shape on the discharge process of Li-ion batteries can be found in [43].

In real world applications, the topology and geometrical shape of the designed microstructure substantially influence the effective transport properties as well as temperature and species distributions in porous media. Peterson [44] aimed at correlating mass transport properties to porous electrode microstructure for Li-ion and alkaline batteries through a combined experimental and modeling approach. The proposed methodology led to enhanced understanding about the connection between microstructure, fundamental principles and cell performance. Oehler et al. [45] presented a numerical and analytical framework to estimate the thermal conductivity as a function of the morphology of the electrode structures (e.g. porosity, particle size distribution, particle shape and particle contact areas). Ioannidis et al. [46] mentioned that information regarding void space distribution is missing in porosity. Accordingly, the authors introduced the autocorrelation as a factor including such information to improve the predictions for reservoir permeability. The importance of the autocorrelation factor in capturing microstructural effects on fluid–thermal transport properties of porous materials was also highlighted by Bodla et al. [47]. Epting et al. [48] showed that incorporating agglomerate diameter distribution can influence the agglomerate model prediction in the case of polymer electrolyte fuel cells by 70%. Zhang et al. [49] developed an experimentally verified numerical framework using 3D pore-scale LB model to investigate the impact of porous structure on the coupled transport and reaction processes in porous electrodes. The aim was to propose guidelines to optimally design microstructures for redox flow battery applications.

Many electrochemical devices constitute thin electrodes, that is, electrodes whose through-plane dimension (thickness) is much smaller than the in-plane dimensions. In such applications, the transport of heat and ions are influenced remarkably by the finite-size effects, because the electrode thickness and solid-phase obstacle size become comparable. To investigate such effects, the transport phenomena should be simulated comprehensively at the pore-scale. The literature review reveals that in the field of heat and mass transfer in porous electrodes, the vast majority of the studies at the pore-scale have been focused on one transport phenomenon. Integrated modeling frameworks for heat, mass and charge transfer in electrochemical systems have been performed under specific assumptions at the cell level (see for instance Ref. [50]). The work by Hwang and Chen [51] proposed a heat/mass coupled modeling approach inside the porous electrodes of fuel cells.

Their research, however, was conducted for a typical porous electrode and information regarding geometrical design and its influence on the transport phenomena and therefore guidelines for future design of porous materials were missing. In this research we aim at filling the knowledge gap by providing a fundamental basis to comprehensively evaluate the microstructural design and the finite-size effects on heat and mass transfer in porous electrodes. The focus of this work is on extensive analysis of the temperature and species distributions within the porous electrodes as well as extracting the effective transport properties (conduction and diffusion coefficients) that are dependent on the ratio of the obstacle size (active material particle diameter) to the system size (the electrode thickness). Furthermore, concerning mass transfer performance in the porous electrodes, none of the previous studies introduced an analytical expression considering finite-size effects. In the current work, we introduce a new tortuosity–porosity correlation to address the pore-scale mass transport inefficiencies at the electrode level. The proposed formula is able to enhance the predictability and accuracy of future system-level simulations. To this aim, the paper is structured as follows: first in Section 2, the LBM for pore-scale simulations of heat and mass transfer is formulated and the microstructural characteristics are provided. In Section 3, the LBM predictions for heat and mass transfer are presented and discussed. Furthermore, we compare and verify our findings by the analytical and empirical correlations found in the literature. Subsequently, the appropriateness of the commonly used simplified effective transport relations for further development of macro-homogeneous models is elaborated and accordingly a novel analytical model is proposed to extract the effective mass-transfer coefficient in porous electrodes. Moreover, via a systematic assessment, guidelines for future design of efficient porous electrodes for electrochemical systems applications are provided. Finally, this study is concluded in Section 4 and the scope of our future research is summarized.

2. Methodology

In Section 2.1, we firstly encapsulate the general formulation of the LBM for solving conductive heat transfer and diffusion problems in porous electrode applications. Section 2.2 describes the electrode reconstruction and presents the factors used to characterize the porous microstructure. In the end, the correlation between the effective transport properties and the temperature and concentration distributions is recapitulated in Section 2.3.

2.1. LBM for pore-scale heat and mass transfer

The pore-scale heat and mass transfer simulations are carried out under the following assumptions: (i) the conductive heat transfer and ionic diffusion phenomena are considered here and therefore the velocity vector is set to zero; (ii) the effect of solute transport and temperature on the fluid velocity and its properties are negligible; (iii) there is no electrochemical reaction at the solid/fluid interface; (iv) the solid phase only consists of active materials and the effects of binders and conductive carbon additives are negligible and (v) the simulations proceed until the steady-state condition is reached.

The LBM is used to solve the governing equations of the conductive heat transfer and ion diffusion in this work. The divergence form of the energy conservation equation in porous media is [52]:

$$\rho c_p \frac{\partial T}{\partial t} = \nabla \cdot (k \nabla T), \tag{3}$$

where ρ is density, c_p is the specific heat, T is the local temperature at time t and k is the thermal conductivity.

Here the single relaxation time (BGK) LB equation for the conductive heat transfer problem is used as [53]:

$$f_{i,h}(\mathbf{x}+\mathbf{e}_i\delta t, t+\delta t) - f_{i,h}(\mathbf{x},t) = -\frac{1}{\tau}\left[f_{i,h}(\mathbf{x},t) - f_{i,h}^{eq}(\mathbf{x},t)\right] + \delta t \cdot \mathbf{F}_{i,T}, \tag{4}$$

Table 1
Solid and fluid transport properties.

Property	Solid	Fluid	References
Thermal conductivity, k (W/(m K))	5	0.18	[19,56]
Heat capacity, c_p (J/(kg K))	632	1642	[19,57]
Density, ρ (kg/(m^3))	1860	1200	[19,58]

where $f_{i,h}$ is the distribution function in the ith direction, $\mathbf{x} = (x, y, z)$ is the spatial position, $\mathbf{e}_i$ is the discrete velocity in the lattice direction i, τ is the dimensionless relaxation time and the vector $\mathbf{F}$ includes sources and external forces.

The equilibrium distribution function along the ith direction ($f_{i,h}^{eq}$) is represented by [37]:

$$f_{i,h}^{eq}(\mathbf{x},t) = \omega_i T(\mathbf{x},t), \tag{5}$$

where ω_i is the weight factor for the lattice structure and finally:

$$T(\mathbf{x},t) = \sum_i f_{i,h}. \tag{6}$$

Karani and Huber [37] proposed the following formulation to include the source term S_{conj} in Eq. (4):

$$\mathbf{F}_{i,T} = \omega_i S_{conj}, \tag{7}$$

$$S_{conj} = \frac{\partial}{\partial x_j}\left(\frac{1}{\rho c_p}\right) \cdot q_j, \tag{8}$$

where the flux q_j can be locally calculated as:

$$q_j = (\rho c_p) \cdot \left[\left(1 - \frac{1}{2\tau}\right)\sum_j \left(f_{j,h} - f_{j,h}^{eq}\right) e_j\right]. \tag{9}$$

With regard to mass transfer, the Nernst–Planck equation governs the movement of ions under the presence of concentration gradients and electric fields [54]. Accordingly, the diffusion form of the ion transport in porous electrodes by assuming that the migration due to the electric field is negligible compared to other transport mechanisms is simplified to the Fick's second law of diffusion as [55]:

$$\frac{\partial c}{\partial t} = \nabla \cdot (D \nabla c), \tag{10}$$

where c is the local concentration at time t and D is the intrinsic diffusion coefficient.

The discretization of the Boltzmann equation for the case of momentum transport takes similar form as Eq. (4). Here we follow the work by Maggiolo et al.[38] to account for the momentum transport equilibrium distribution ($g_{i,m}^{eq}$) as:

$$g_{i,m}^{eq}(\mathbf{x},t) = \omega_i \rho. \tag{11}$$

The local concentration $c(\mathbf{x},t)$ is obtained from the first hydrodynamic moment of this second lattice population g_i as:

$$c(\mathbf{x},t) = \sum_i g_i. \tag{12}$$

Table 1 summarizes heat and mass transport properties for the solid and fluid phases used in simulations.

2.2. Geometry construction and microstructural characteristics

The 3D geometry of the porous electrode under study belongs to the anode electrode of a commercial high energy Li-ion cell. The solid phase constitutes overlapping spherical graphite particles randomly distributed in a cuboid representing the electrode compartment. The void space of the electrode is filled by ethylene carbonate-based organic solution to facilitate ions transfer within the porous structure. In this work two scenarios are considered for the ratio of the obstacle size (particle diameter) to the system size (electrode thickness) to evaluate the finite-size effects on heat and mass transport properties of the microstructure.

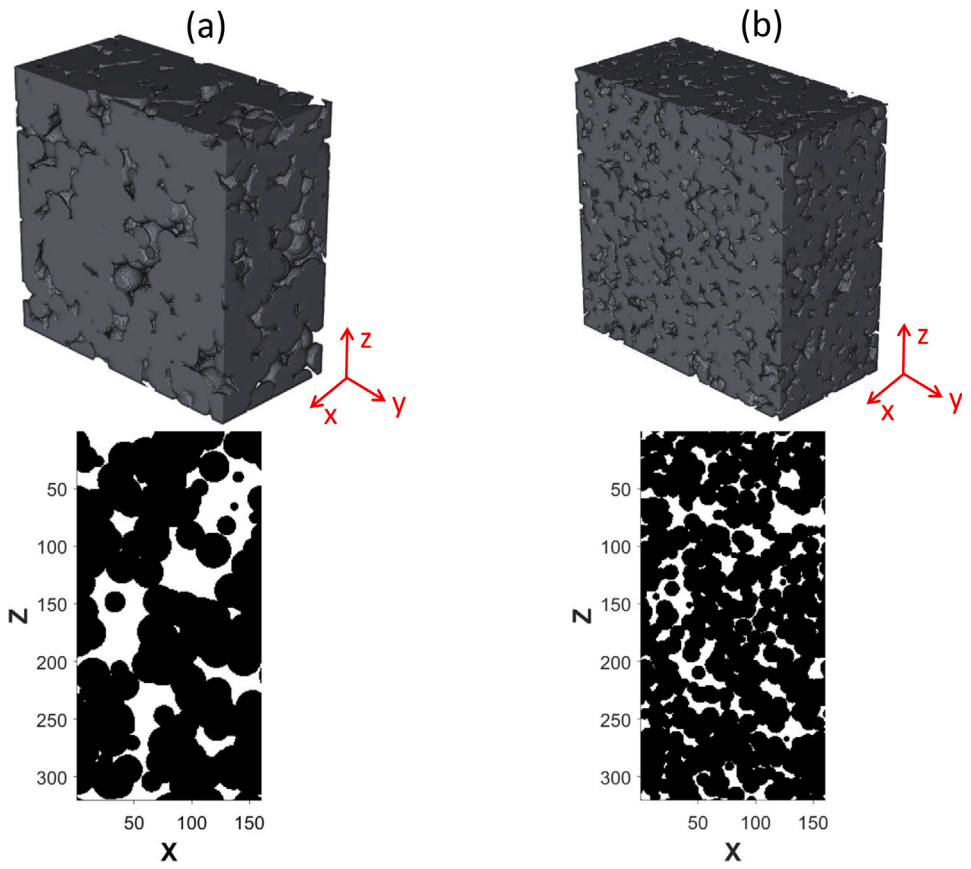

Fig. 1. Representative 3D and 2D images for the electrode microstructure. **(a):** Top: 3D view of the porous electrode made up of large particles where d/L_x=0.2; Bottom: $z-x$ cross-sectional view of the porous electrode made up of large particles at the middle of the y axis. **(b):** Top: 3D view of the porous electrode made up of small particles where d/L_x=0.1; Bottom: $z-x$ cross-sectional view of the porous electrode made up of small particles at the middle of the y axis.

A 3D volume with the size of $(L_x \times L_y \times L_z)$=(160 × 320 × 320) voxels has been selected to construct the electrodes, where x represents the flow direction along the thickness of the electrode. The first and the second cases (hereafter are denoted by *Large Particles* and *Small Particles*) differ with respect to the particle diameter, d. The d/L_x ratio for *Large Particles* is 0.2 and equals 0.1 for the *Small Particles*. Fig. 1 represents the 3D structure of the porous electrodes together with corresponding two-dimensional (2D) $x-z$ images at $y=160$ where a periodic boundary condition has been imposed in all three directions.

The void space structure in the porous medium can be identified by the local values (at $\vec{r}$) of the phase function $Z(\vec{r})$. The phase function either equals zero or one depending on whether the point $\vec{r}$ falls in the solid phase or the fluid, respectively. Following the works by Ioannidis et al. [46] and Bodla et al. [47], here the porosity (ϕ) and the autocorrelation ($R_z(\vec{l})$) are considered as the first two statistical moments of the phase function utilized to describe the statistical porous media as:

$$\phi = \overline{Z(\vec{r})}, \tag{13}$$

$$R_z(\vec{l}) = \frac{\overline{\left[Z(\vec{r})-\phi\right]\left[Z(\vec{r}+\vec{l})-\phi\right]}}{\left[\phi-\phi^2\right]}. \tag{14}$$

In this work, three different random seeds are considered in the geometry reconstruction algorithm to account for the effect of randomness in generating the microstructure 3D matrices. The electrode porosity is kept constant in all of the studied cases at 0.16 which replicates Li-ion battery cells with high specific energy. The autocorrelation function ($R_z(\vec{u})$) on the other hand implicitly describes the void space distribution and measures the spatial correlation degree among the points occupied by the fluid phase (i.e. the pore network).

Pore size identification is not a straightforward task. In this work, we firstly define the equivalent pore diameter (d^{eq}_{pore}) as the diameter of a sphere having the same volume as the void space (V_{pore}):

$$d^{eq}_{pore} = \sqrt[3]{\frac{6V_{pore}}{\pi}}. \tag{15}$$

Subsequently, the probability distribution function (PDF) of d^{eq}_{pore} is provided for the constructed geometries. To this aim, the kernel density estimation (KDE) has been selected to predict the probability density function of the randomly generated porous structures. Fig. 2 illustrates the KDE for the normalized d^{eq}_{pore} with respect to the particle diameter d. The shaded regions graphically represent the standard errors over the average values and reflect the impact of randomness on the pore size distributions. The average pore size diameter (in voxels) is 8.2 (i.e. $d^{avg}_{pore}/d_{particle}$=0.26) for the case with large particles and 4 (i.e. $d^{avg}_{pore}/d_{particle}$=0.25) for the case constituting small particles. However, the number-based distributions (see Fig. 2-(a)) do not contain information about the volume share of pores with specific size in the porous medium. Therefore, Fig. 2-(b) presents the volume-weighted KDE to provide such details. The relation between the number- and volume-weighted distributions is formulated as:

$$KDE^{v}_{i} = \frac{(d^{eq}_{pore,i})^3}{\sum_i (d^{eq}_{pore,i})^3} KDE^{n}_{i}, \tag{16}$$

where the superscripts v and n represent the volume-weighted and the number-based KDEs, respectively. As Fig. 2-(b) shows, by applying the volume-weighting approach, the observed peaks in the KDEs shift towards pores of medium size and the average pore diameters (in voxels) are 15.2 (i.e. $d^{avg}_{pore}/d_{particle}$=0.48) and 7.3 (i.e. $d^{avg}_{pore}/d_{particle}$=0.46) for the cases with large and small particles, respectively.

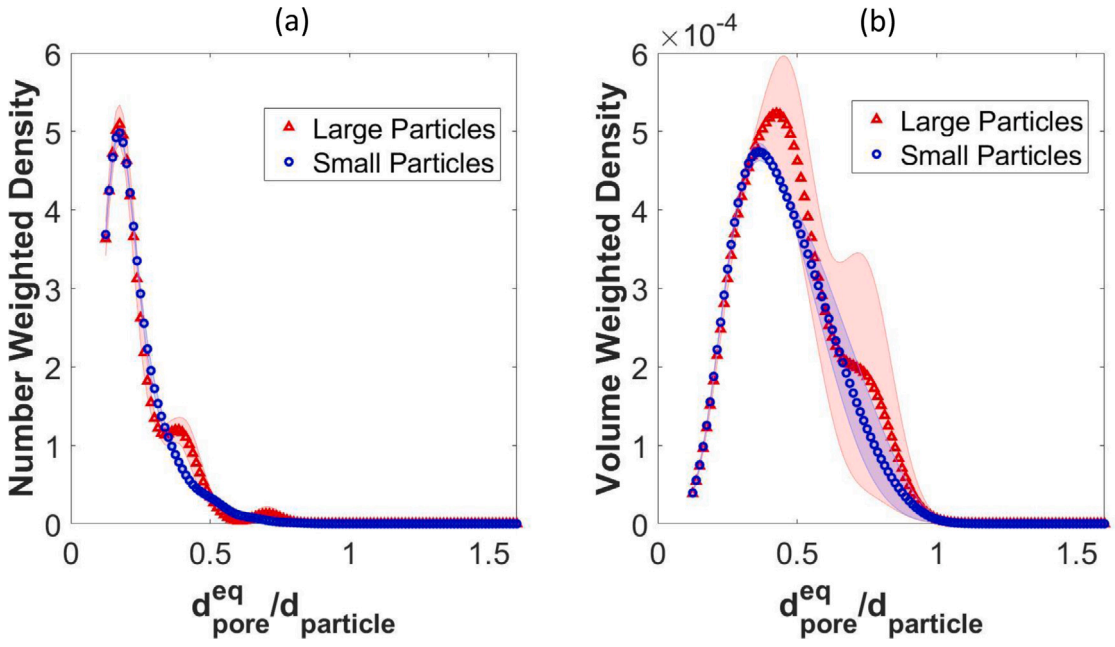

Fig. 2. Pore size distributions. **(a):** Number-weighted KDEs; for the case with large particles $d^{avg}_{pore}/d_{particle}$=0.26 and for the case with small particles $d^{avg}_{pore}/d_{particle}$=0.25. **(b):** Volume-weighted KDEs; for the case with large particles $d^{avg}_{pore}/d_{particle}$=0.48 and for the case with small particles $d^{avg}_{pore}/d_{particle}$=0.46.

As mentioned earlier, the autocorrelation function (see Eq. (14)) is another way for characterizing porous microstructures. As can be seen in Fig. 3, the autocorrelation is equal to unity for very small lags and approaches zero by increasing the lag. Moreover, it is observed that as the lag length increases, the difference between the autocorrelation functions at x, y and z directions becomes more pronounced for the case with large particles compared to the small particles. Koza et al. [59] mentioned that for the porous media studied in their work, the finite-size anisotropy effect was negligible when the ratio of the obstacle to the system size (d/L) was smaller than 0.01. In our work, this ratio is 0.2 and 0.1 for the cases with large and small particles, respectively. Therefore, our observation of the dependence of finite-size effects on the d/L ratio (the directional dependence of the autocorrelation) is aligned with the findings by Koza et al. [59].

Typically an exponentially decaying function is used to fit the autocorrelation data and to extract the correlation length of a porous structure [46,47], as:

$$R_z(\vec{l}) = exp\left[-\left(\frac{l}{\lambda}\right)^n\right], \tag{17}$$

where λ and n are the fitting coefficients. The parameter λ is the correlation length which characterizes the length scale of the spatial structure. By fitting Eq. (17) to the autocorrelation data shown in Fig. 3, the average correlation length (λ in voxels) for the case with large particles is 10.3 (i.e. $\lambda/d_{particle}$=0.32) and equals 5.8 (i.e. $\lambda/d_{particle}$=0.36) when the porous structure is made up of small particles. These values are approximately similar to those obtained based on number-based pore size distributions (i.e. $d^{eq,avg}_{pore}$). It is worth mentioning that the $\lambda_{large}/\lambda_{small}$ ratio is 1.8 which is, as expected, approximately the same as the ratio between the particle sizes (d_{large}/d_{small}=2).

2.3. Validation

To extract the effective thermal conductivity, the conductive heat transfer problem formulated in Section 2.1 is numerically solved by LBM considering pre-defined temperature boundary conditions on the two opposing faces along the cell thickness ($T^*(x=0)=1$ and $T^*(x=L_x)=0$). The effective thermal conductivity is subsequently calculated by volume-averaging the localized heat fluxes in the porous structure after having reached the steady-state condition, as [31]:

$$\frac{k_{eff,x}}{k_s} = \frac{\int\left((1-\phi(x,y,z))\frac{\partial T(x,y,z)}{\partial x} + \frac{k_f}{k_s}\phi(x,y,z)\frac{\partial T(x,y,z)}{\partial x}\right)dxdydz}{\left(\frac{T_L-T_0}{L_x}\right)L_xL_yL_z}, \tag{18}$$

where k_{eff}, k_s and k_f stand for the effective, solid phase and fluid phase thermal conductivities, respectively.

To evaluate the accuracy of the employed numerical method, here we compare the predictions for the effective thermal conductivity calculated numerically with the analytical solution provided by the inverse rule of mixtures (iROM). The iROM theory applies to the serially connected composite materials when each phase is assumed to be contiguous and is placed perpendicular to the direction of the heat flow [3,60]. For a porous two-phase system, the k^{iROM}_{eff} is obtained as:

$$\frac{1}{k^{iROM}_{eff}} = \frac{\phi}{k_f} + \frac{1-\phi}{k_s}. \tag{19}$$

Since in this work the low-porous electrode is of interest, the accuracy of the numerically calculated effective thermal conductivity is controlled by the number of the computational nodes in the fluid phase. We assume different 1D geometries with fixed porosity ($\phi = 0.16$) to investigate the influence of the number of the computational nodes in the liquid phase on the relative change (RC) between the effective thermal conductivities computed numerically (k^{LBM}_{eff}) and using the iROM approach (k^{iROM}_{eff}), where:

$$RC(\%) = \frac{\left|k^{LBM}_{eff} - k^{iROM}_{eff}\right|}{k^{iROM}_{eff}} \times 100. \tag{20}$$

Fig. 4 shows that increasing the number of the nodes in the liquid phase from 5 to 30 reduces the relative change in k_{eff} from 22.4% to 3.9%, respectively. The improvements in the numerical solution is though less pronounced when the number of the considered nodes exceeds 15. As mentioned earlier by analyzing Fig. 2-(b), the average pore diameters (in voxels) are 15.2 and 7.3 for the cases with large and small particles, respectively. Such number of computational nodes in the fluid phase leads to a good compromise between accuracy (i.e. RC<15%) and computational cost.

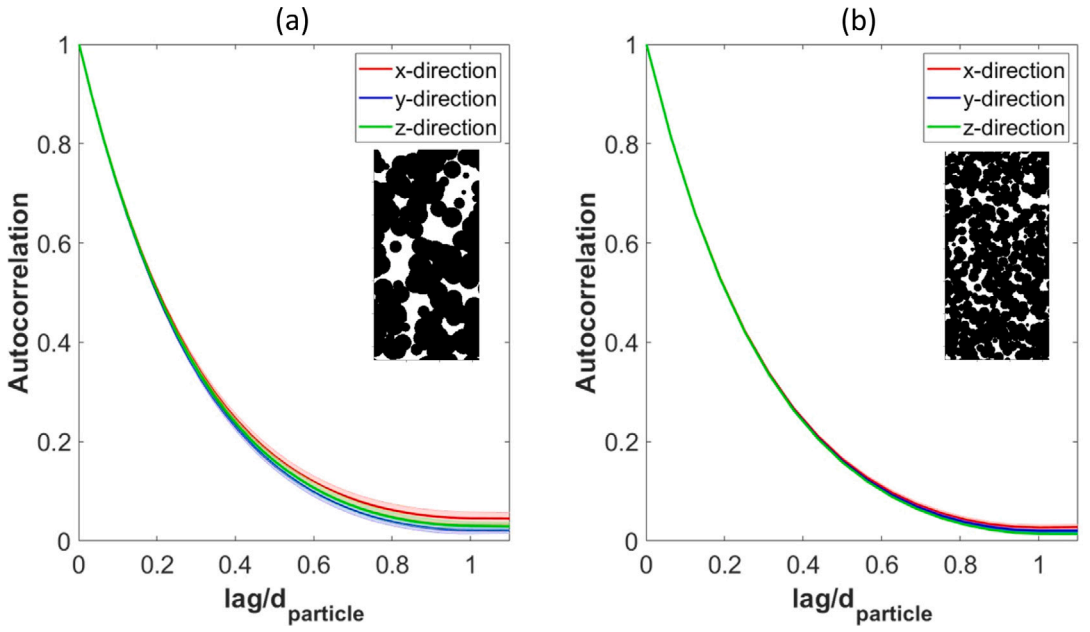

Fig. 3. Autocorrelation factor versus the normalized lag length. **(a):** The microstructure made up of large particles where the finite-size anisotropy effects are more pronounced and $\lambda_x/d_{particle}$=0.32. **(b):** The microstructure made up of small particles where the finite-size anisotropy effects are less pronounced and $\lambda_x/d_{particle}$=0.36.

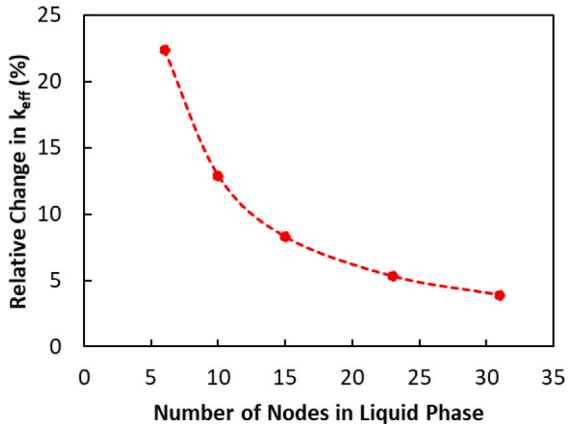

Fig. 4. Relative change between the numerical- and iROM-based k_{eff} by the number of the liquid nodes.

Similarly, the 3D concentration profile within the porous structure is obtained by solving for the Fick's law of diffusion using LBM considering the relevant concentration boundary conditions along the cell thickness ($c^*(x=0)=1$ and $c^*(x=L_x)=0$). Following He et al. [55], the effective diffusivity $D_{eff,x}$ is calculated by volume-average of the diffusion fluxes at steady-state condition as:

$$\frac{D_{eff,x}}{D_f} = \frac{\int_{V_f}\left(\frac{\partial c(x,y,z)}{\partial x}\right)dxdydz}{\left(\frac{c_L-c_0}{L_x}\right)L_xL_yL_z}, \tag{21}$$

where D_f is the molecular diffusion coefficient within the fluid phase and V_f stands for the fluid volume.

3. Results and discussion

In this section, the LBM simulation results for heat and mass transfer (Sections 3.1 and 3.2) are elaborated and our numerical observations are compared with relevant analytical/empirical correlations found in the literature. Lastly, Section 3.3 provides guidelines for future design of porous electrodes. In this section, we have selected the first randomization seed (rnd_1) to visualize the 3D distributions and contour plots of temperature and concentration within the porous structures.

3.1. LBM simulation results for heat transfer

Fig. 5 presents the 3D temperature plots at the steady-state condition resulting from the implementation of LBM to the pore-scale conductive heat transfer problem formulated in Section 2.1. The effective thermal conductivities and the KDEs of the temperature distributions are presented here to elaborate the effectiveness of heat transfer within differently designed microstructures.

Fig. 6 illustrates the average planar temperature profile and the KDEs of temperature distributions for both microstructures made up of the large and small particles. It is observed from Fig. 6-(a) that both cases experience approximately similar linear patterns in average temperature profiles along the electrode thickness. The solid lines in Fig. 6-(b) replicate the average KDE values of temperature over the three investigated random geometries. Results show that the standard deviations of the afore-stated average profiles are 0.035 and 0.015 for the cases with large and small particles, respectively. In other words, the case constituting large particles depicts more variations in local temperatures compared to the other geometry with small particles. To quantify the randomness effect on the temperature distributions, the average value for the standard deviations of KDEs at each temperature slot has been calculated. The case with large particles is more sensitive to the randomization (avg_{stdv} = 0.031) compared to the case with small particles (avg_{stdv} = 0.017). The shaded error bar regions over the average quantities represents the randomness effect on temperature distributions graphically.

Table 2 summarizes the k_{eff} with respect to the solid phase thermal conductivity for different design cases under study. Results are aligned with the findings from the average temperature profiles already shown in Fig. 6-(a). This is due to the fact that k_{eff} is extracted by volume-averaging of the local heat fluxes (see Eq. (18)). There is around 2% difference in k_{eff} values obtained from the cases with large and small particles. It is concluded that at the macroscopic level (we consider k_{eff} as a macroscopic property at the electrode scale), decreasing the particle size to one half of its original value does not contribute to significant changes. However, as discussed, the pore-scale temperature

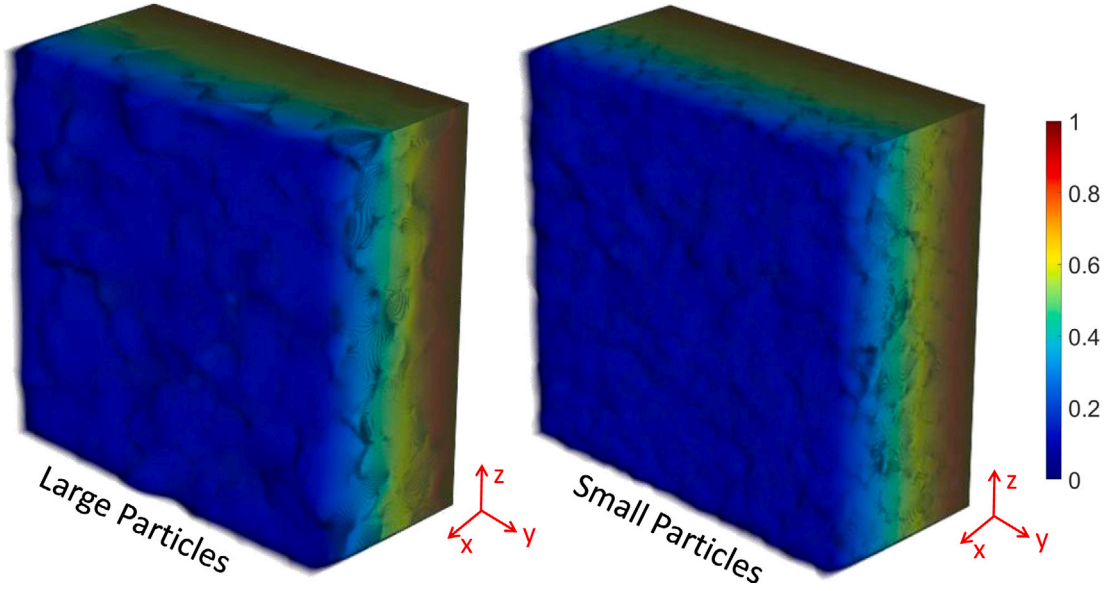

Fig. 5. 3D temperature distributions within the porous structure. Left: The porous electrode made up of large particles; Right: The porous electrode made up of small particles.

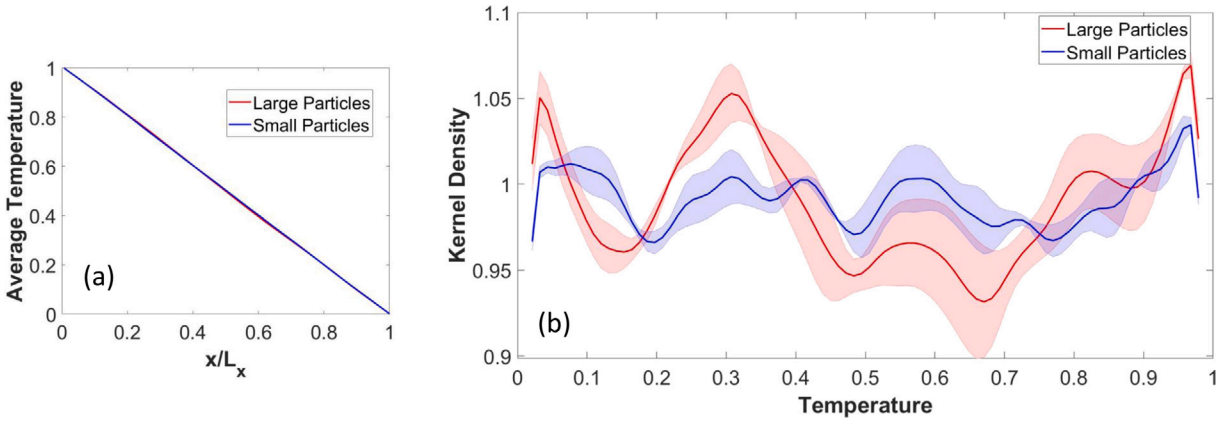

Fig. 6. Temperature profiles within the porous electrode. **(a):** Average planar temperature profile along the electrode thickness where both cases show approximately the same linear profiles. **(b):** KDEs of temperature profiles within the porous structure. The standard deviation of the average temperature profiles are 0.035 and 0.015 for the cases with large and small particles, respectively.

variations are more pronounced and the case with small particles indicates more temperature uniformity within the electrode compared to the case with large particles. Such variations can be linked to the microstructural characteristics where as discussed in Section 2.2, the finite-size anisotropy effects become more evident as the ratio of the particle size to the system size increases. Furthermore, both the average pore equivalent diameter and the correlation length are larger for the case with large particles than the case with small particles. Since the thermal conductivity of the fluid phase is remarkably lower than the solid phase, this leads to the presence of some localized thermal resistances and in turn temperature nonuniformities. Fig. 7 visualizes the "$z - x$" temperature contour plots at three different "y" cross sections. This figure provides a closer view of the localized temperature distributions and the more uniform temperature patterns yielded from constructing the microstructure made up of small particles.

Table 3 provides a comparison of the numerically extracted effective thermal conductivity based on LBM in this work with the predictions by oft-used Bruggeman correlation [61], and its modified version [31], as well as the Effective Medium Theory (EMT) for completely random distribution of components [3]. Our results are very well supported by the values found in the literature by considering the same porosity and material properties. The relative difference between the average value of the effective thermal conductivities extracted from the literature and the average value calculated numerically in our study is 0.22%. Eq. (23) is an experimentally developed correlation for the effective thermal conductivity proposed by Vadakkepatt et al. [31]. The relative error between the numerically calculated thermal conductivity in our work compared to the value predicted experimentally by Ref. [31] is 8.9%. Moreover, it is seen that the presented effective thermal conductivity correlations are commonly porosity dependent and the impact of the particle size is not explicitly reflected. Our observations also indicate that there is no significant change in the effective thermal conductivity values as long as the porosity is fixed, even in the case that the particle size is halved.

Table 2
Effective thermal conductivities of the porous media.

Property	rnd_1	rnd_2	rnd_3	Average
k_{eff}^{large}/k_s	0.736	0.742	0.736	0.738
k_{eff}^{small}/k_s	0.752	0.750	0.752	0.751

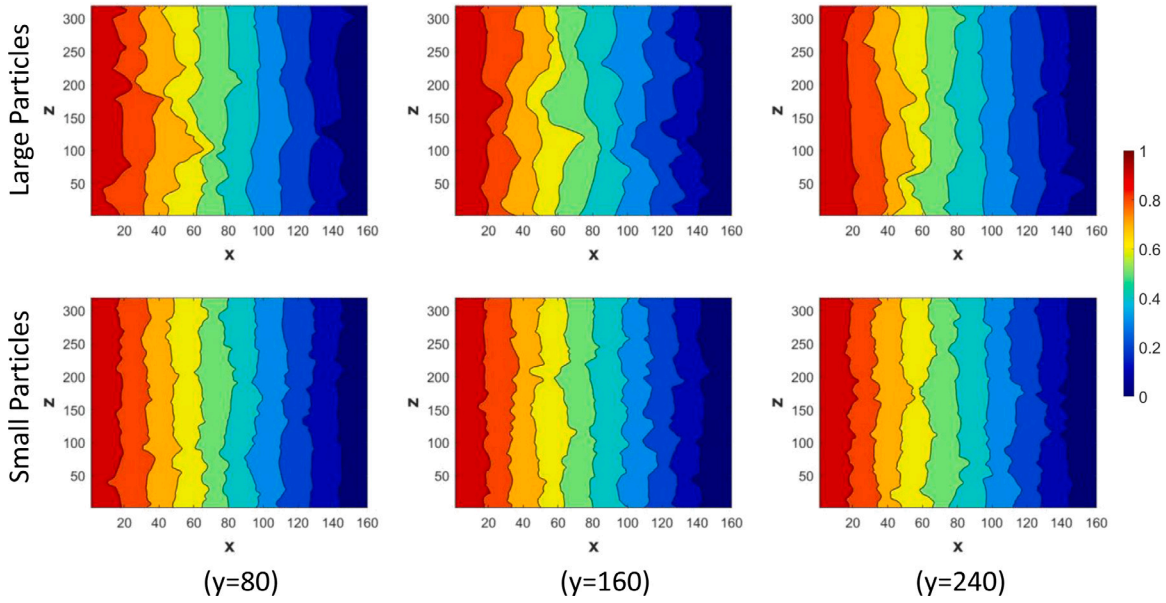

Fig. 7. 2D temperature contour plots at y=80; y=160 and y=240 cross sections within the porous electrode. Top: The microstructure made up of large particles experiences less uniform temperature profiles; Bottom: The microstructure of small particles shows more uniformity in temperature profiles.

Table 3
Comparison with literature for the effective thermal conductivity.

Correlation	Formulation		Large/Small	Reference
Bruggeman	$k_{eff} = k_s(1-\phi)^{1.5} + k_f(\phi)^{1.5}$	(22)	3.86	[61]
Modified Bruggeman	$k_{eff} = k_s(1-\phi)^{2.2} + k_f(\phi)^{1.5}$	(23)	3.42	[31]
EMT	$(1-\phi)\frac{k_s-k_{eff}}{k_s+2k_{eff}} + (\phi)\frac{k_f-k_{eff}}{k_f+2k_{eff}} = 0$	(24)	3.87	[3]
This work	Eq. (18)		3.69/3.76	

Table 4
Effective diffusivities and the tortuosity factors for the porous media.

Property	rnd_1	rnd_2	rnd_3	Average
D_{eff}^{large}/D_f	0.041	0.044	0.041	0.042
τ_{large}	3.90	3.64	3.90	3.81
D_{eff}^{small}/D_f	0.034	0.035	0.035	0.035
τ_{small}	4.71	4.57	4.57	4.62

Table 5
Comparison with literature for the tortuosity factor.

Correlation	Formulation		Large/Small	Reference
Bruggeman	$\tau = \phi^{-1/2}$	(25)	2.5	[24]
Modified Bruggeman	$\tau = 1.8\phi^{-0.53}$	(26)	4.8	[29]
Elias-Kohav	$\tau = \phi^{-1}$	(27)	6.25	[2]
This work (numerical)	Equations (1) and (21)		3.8/4.6	

3.2. LBM simulation results for mass transfer

The 3D concentration distributions within the void space of the porous electrodes are depicted in Fig. 8. To assess the capability of the generated geometries in transferring ions within the fluid phase, the effective diffusivities and in turn the tortuosity of the porous electrodes are computed. In addition, the standard deviations of the concentration distributions at the pore-scale are quantified.

Fig. 9-(a) illustrates that the difference between the average planar concentration profiles between the cases with large and small particles are more obvious compared to the corresponding temperature profiles (see Fig. 6-(a)). To reflect this quantitatively, Table 4 provides the effective diffusivities with respect to the intrinsic molecular diffusivity of the fluid phase as well as the tortuosity factor by volume-averaging the local diffusion fluxes (see Eqs. (1) and (21)). It is seen that the case with large particles shows 20% higher effective diffusivity compared to the case with small particles. This highlights that the change in the particle size influences the mass transfer at the macroscopic level further than the heat transfer performance as discussed previously in Section 3.1.

The ratio of the intrinsic molecular diffusivity to the effective mass transfer coefficient of the porous medium is linked to the tortuosity factor (see Eq. (1)). The numerically obtained tortuosities using LBM and by applying Eqs. (1) and (21) in this study together with the values calculated based on other approaches reported in the literature are summarized and compared in Table 5. It is seen that the commonly used Bruggeman correlation (Eq. (25)) in macro-homogeneous modeling of electrochemical systems, underestimates the tortuosity factor substantially compared both to our observations and using the approaches reported by Refs. [2,29]. The modification on the Bruggeman correlation (Eq. (26)) yielded to an appropriate fit to the experimental observations for various types of electrodes as discussed by Thorat et al. [29]. The relative error between the numerically calculated tortuosity in our work for the case consisting small particles compared to the value predicted experimentally by Ref. [29] is 4.2%. However, the proposed modified relation offered by Thorat et al. [29] is only porosity dependent and does not consider the particle size or the finite-size effects.

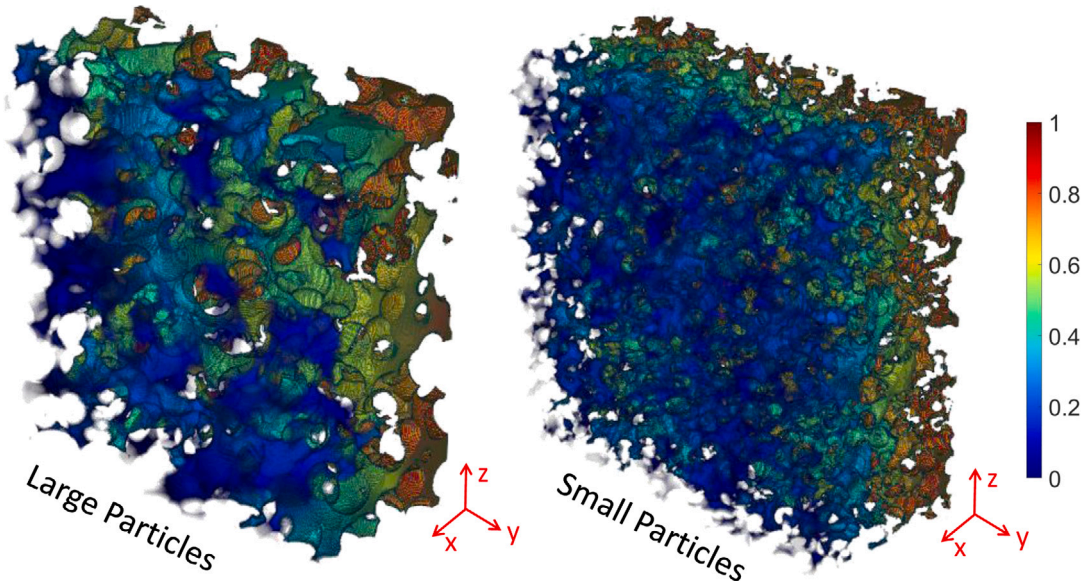

Fig. 8. 3D concentration distributions within the fluid phase. Left: The porous electrode made up of large particles; Right: The porous electrode made up of small particles.

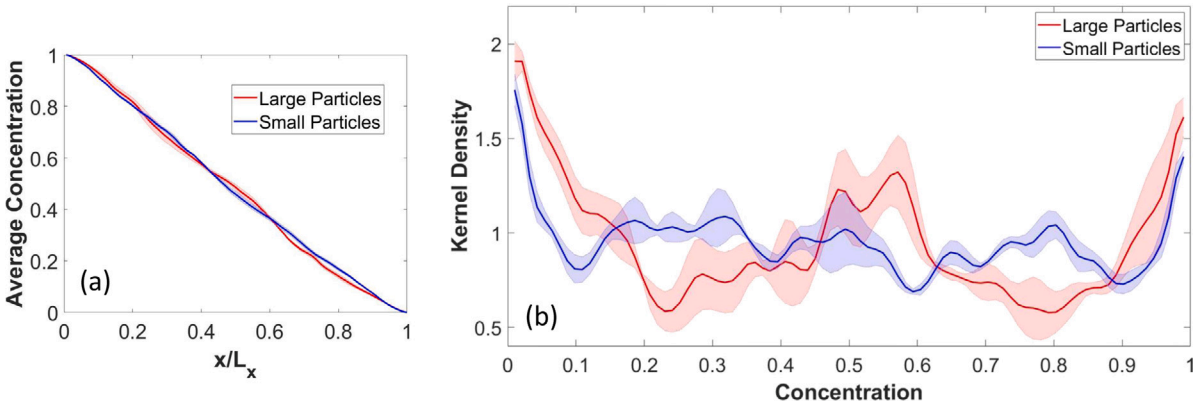

Fig. 9. Concentration profiles within the porous electrode. **(a):** Average planar fluid phase concentration profile along the electrode thickness. The case with large particles shows more nonlinear planar concentration profile compared to the case with small particles. **(b):** KDEs of concentration profiles within the porous structure. The standard deviation of the average concentration profiles are 0.31 and 0.17 for the cases with large and small particles, respectively.

The tortuosity factor for a completely random arrangement is approximated by the number of diffusional steps (m) taken by the random walk algorithm as [2]:

$$\tau = 1 + (1-\phi) + (1-\phi)^2 + \cdots + (1-\phi)^m. \tag{28}$$

For sufficiently large number of diffusional steps: $\tau = 1/\phi$. However, in thin electrode applications m holds finite values. Therefore, we aim at proposing a tortuosity–porosity correlation for thin porous electrodes where the finite-size effects are influential. To this end, it is assumed that the number of diffusional steps equals the dimensionless system length (i.e. $m = L_x/d$). Thereby by considering the original version of Eq. (28) and by further simplification using power series, the tortuosity reads as:

$$\tau = 1 + \sum_{k=1}^{m}(1-\phi)^k = \frac{1-(1-\phi)^{m+1}}{\phi}. \tag{29}$$

Based on Eq. (29), for the cases with large and small particles the tortuosity is 4.05 and 5.3, respectively. The predictions obtained by Eq. (29) are well aligned with both our numerical findings and the experimentally driven modified Bruggeman correlation offered by Thorat et al. [29] (see Table 5). The afore-stated modification yields a computation of the tortuosity for the porous electrodes that embeds finite-size effects and proposes a more accurate and comprehensive substitute for the oft-used Bruggeman relation in macro-homogeneous modeling of electrochemical cells.

The tortuosity is inversely proportional to the ratio of the particle diameter to the electrode thickness (d/L_x). Our findings are in alignment with the work by Duda et al. [62], where the following power law dependency was proposed to correlate the tortuosity to the so-called dimensionless system length (L_x/d):

$$\tau \propto \left(\frac{L_x}{d}\right)^{0.19}. \tag{30}$$

Eq. (30) predicts that $\tau_{small}/\tau_{large}$ is 1.14 which is in good agreement with the results obtained by both our analytical model and numerical investigations where this ratio equals 1.31 and 1.21, respectively.

Fig. 9-(b) presents the KDE as a measure to visualize the concentration distributions within the electrodes under investigation. The standard deviations of the average KDEs (solid lines in Fig. 9-(b)) are 0.31 and 0.17 for the cases with large and small particles, respectively. Furthermore, quantification of the impact of randomness on the concentration distributions reflects that the average value for the concentration KDEs (avg_{stdv}) are 0.21 and 0.12 for the cases with large and small particles, respectively. Therefore, it is concluded that the case with large particles experiences more nonuniformity in concentration distribution within the porous structure compared to the case having small particles.

3.3. Systematic discussion and guidelines for future design of porous electrodes

In this section we systematically analyze the outcomes of this study and propose solutions for novel electrode design exploration. The finite-size effects on heat and mass transfer in porous electrodes were investigated at both the macro and micro scales. The effective transport properties were considered as the macro properties at the electrode level since they link the microstructural effects to the well established macro-homogeneous electrochemical models. At the micro level, the distributions of temperature and concentration were extracted at the pore-scale and the observed variations were quantified for the cases under study.

Analysis of the results at the macro level shows that there is no significant difference in the effective thermal conductivity when the ratio of the obstacle size (particle diameter) to the system size (electrode thickness) is halved. However, this change leads to 21.1% increase in the tortuosity factor (i.e. reduction in the effective diffusivity) for the case with small particles compared to the case constituting large particles. Therefore, the mass transfer is more influenced by finite-size effects in comparison with the heat transfer in porous media. This phenomenon is due to the fact that heat flows both through the solid and the fluid phases while it is only the fluid phase which contributes to the transfer of ions within the electrode compartment.

The above-referenced macro scale investigations provide valuable inputs to the system-level simulations. However, when the electrochemical devices are examined at the electrode level, issues such as uneven distributions of temperature and species concentrations can potentially give rise to localized effects (e.g. hotspots and nonuniform electrochemical reactions), performance deterioration and eventually to thermal runaways under extreme conditions. Therefore, to prevent such undesired phenomena, it is essential to further capture and assess the impact of the microstructure on the uniformity of temperature and concentration profiles within the porous electrode. Analyzing the results of this research at the micro level by referring to Fig. 10, shows that for both the heat transfer and mass transport studies, the standard deviation values of KDEs for the case with large particles are approximately twice the corresponding quantities for the porous medium constituting small particles. In other words, when the microstructure is made up of small particles, the distributions of temperature and concentration are more uniform. However, the average values of the standard deviations for the mass transfer study are approximately ten times the values obtained from the heat transfer study. Therefore, the micro level investigations also confirm the higher sensitivity of the mass transfer to the microstructural effects compared to the heat transfer. Although it was observed that at the macro level (where the local fluxes are volume averaged), the case with large particles had around 20% higher effective diffusivity, at the micro level the case with small particles showed more concentration uniformity since the finite-size anisotropy effects were less pronounced (see Fig. 3).

In the authors' previous study [1], a multi-physics approach was employed to systematically optimize the electrode configuration while considering the interactions between the electrochemical cells and systems under realistic working scenarios. It was concluded that thinner electrodes are superior compared to the commercially available thick electrodes both from the energy efficiency and the thermal performance perspectives. In the current work, it was observed that the finite-size anisotropy effects are of crucial importance when the ratio of the obstacle size to the system size increases. In terms of uniformity of the temperature and concentration distributions, the electrode made up of particles of smaller size experienced improved transport capabilities. Therefore, the development of active materials constituting smaller particles seems to be beneficial both from the micro level and the system level points of view. However, as highlighted by Liu et al. [63], the small particles increases the electrode active surface area for the side reactions which in long-term may lead to accelerated degradation. These facts bring forth the development of the advanced multi-scale multi-physics frameworks together with model hybridization techniques to provide deeper insights for the performance assessment of thin electrodes at different scales and to propose novel design alternatives. As a starting point in this context, this work provided microstructural dependent feedbacks to the macro-homogeneous electrochemical models by correlating the effective transport properties to the electrode microstructure. Most importantly, the developed framework here made it possible to comprehensively investigate the temperature and concentration distributions within the porous structure and to provide insights for future development of efficient porous electrodes.

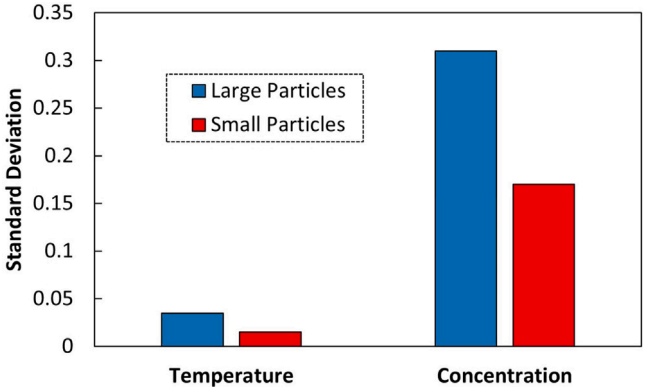

Fig. 10. Standard deviation values of KDEs for the temperature and concentration distributions. The standard deviation values for the case with large particles are approximately twice the values obtained from the case with small particles. The average values of the standard deviations for the mass transfer study are around ten times the corresponding values for the heat transfer study.

4. Conclusions

A comprehensive research was carried out to investigate the finite-size effects on heat and mass transfer in porous electrodes. The LBM based numerical approach was proposed to solve the conductive heat transfer and diffusion problems at the pore-scale. The study was focused on the finite-size effects on the transport capability of the porous structure at both the macro (electrode) and micro (pore) levels. To this aim, two kinds of geometries were constructed. The first case constituted large particles while the second case contained small particles with half of the size considered in the first case. At the macro level, the effective transport properties were extracted and the results were compared with the literature. The key findings in this research are listed as follows:

- The relative error between the numerically calculated thermal conductivity in our work compared to the relevant experimental value found in the literature was 8.9%.
- The relative error between the numerically calculated tortuosity in our work for the case consisting small particles compared to the relevant experimental value found in the literature was 4.2%.
- At the micro level, it was found that particles of small size provide more uniform distributions of temperature and concentration within the microstructure with standard deviations of approximately half of the values obtained from the case with large particles.
- A novel tortuosity–porosity correlation was proposed to correlate the effective mass transfer coefficient to the finite-size effects. The proposed analytical relation was considered as a more accurate alternative for the oft-used Bruggeman equation for being used in the macro-homogeneous modeling of electrochemical cells.
- Increasing the particle-to-thickness size of a factor of 2 increased the effective mass transfer coefficient of roughly 20%–30%.

- Both the analyses at the micro and at the macro levels showed that the mass transfer performance is further influenced by the change in the particle size compared to the heat transfer effectiveness.
- The average values of the standard deviations for the concentration KDEs were approximately ten times the values obtained from the KDEs of temperature distributions.
- The systematic assessment proposed the development of active materials constituting particles of small size for manufacturing porous electrodes.

The outcomes of this work highlight that the development of multi-physics multi-scale simulation frameworks in combination with model hybridization techniques is pivotal in the future design of energy and thermally efficient electrochemical systems.

Nomenclature

List of Symbols

c	concentration (mol m^{-3})
c_p	specific heat (J kg^{-1} K^{-1})
d	diameter (in voxels)
D	diffusion coefficient (m^2 s^{-1})
$\mathbf{e}$	discrete velocity
f_h	heat transfer distribution function
$\mathbf{F}$	external forces
g_m	mass transfer distribution function
i	lattice direction
k	thermal conductivity (W m^{-1} K^{-1})
l	lag (in voxels)
L	length (in voxels)
q	local flux
r	local position
R	autocorrelation
S	source term
T	temperature (°C)
t	time (s)
V	volume (in voxels)
$\mathbf{x}$	spatial position
Z	phase function

Greek Letters

α	Bruggeman exponent
δ	time step
λ	correlation length (in voxels)
ρ	density (kg m^3)
τ	tortuosity
ϕ	porosity
ω	weight factor

Subscripts/ Superscripts

eff	effective
eq	equilibrium
f	fluid
h	heat transfer
m	mass transfer
s	solid
$*$	normalized value

Abbreviations

avg	average
iROM	inverse rule of mixtures
KDE	kernel density estimation
LBM	lattice Boltzmann method
Li-ion	lithium-ion
NCM	lithium nickel cobalt manganese oxide
RC	relative change
rnd	random
stdv	standard deviation
3D	three dimensional

CRediT authorship contribution statement

Majid Astaneh: Conceptualization of this study, Methodology, Simulations, Analysis, Writing – original draft. **Dario Maggiolo:** Conceptualization of this study, Methodology, Code development, Analysis, Writing – review & editing. **Henrik Ström:** Project management, Overall guidance, Writing – review & editing.

Declaration of competing interest

The authors declare that they have no known competing financial interests or personal relationships that could have appeared to influence the work reported in this paper.

Data availability

No data was used for the research described in the article.

Acknowledgments

The computations were enabled by resources provided by the Swedish National Infrastructure for Computing (SNIC) at Tetralith (NSC) [64].

Funding

This work has been financially supported by the Swedish Energy Agency (project number P47906-1).

References

[1] M. Astaneh, J. Andric, L. Löfdahl, P. Stopp, Multiphysics simulation optimization framework for lithium-ion battery pack design for electric vehicle applications, Energy 239 (2022) 122092, http://dx.doi.org/10.1016/j.energy.2021.122092, URL https://www.sciencedirect.com/science/article/pii/S0360544221023409.

[2] T. Elias-Kohav, S. Moshe, D. Avnir, Steady-state diffusion and reactions in catalytic fractal porous media, Chem. Eng. Sci. 46 (11) (1991) 2787–2798, http://dx.doi.org/10.1016/0009-2509(91)85148-Q, URL https://www.sciencedirect.com/science/article/pii/000925099185148Q.

[3] J. Wang, J.K. Carson, M.F. North, D.J. Cleland, A new approach to modelling the effective thermal conductivity of heterogeneous materials, Int. J. Heat Mass Transfer 49 (17) (2006) 3075–3083, http://dx.doi.org/10.1016/j.ijheatmasstransfer.2006.02.007, URL https://www.sciencedirect.com/science/article/pii/S0017931006001293.

[4] C.C. Chueh, A. Bertei, J.G. Pharoah, C. Nicolella, Effective conductivity in random porous media with convex and non-convex porosity, Int. J. Heat Mass Transfer 71 (2014) 183–188, http://dx.doi.org/10.1016/j.ijheatmasstransfer.2013.12.041, URL https://www.sciencedirect.com/science/article/pii/S0017931013010855.

[5] P.A. García-Salaberri, Modeling diffusion and convection in thin porous transport layers using a composite continuum-network model: Application to gas diffusion layers in polymer electrolyte fuel cells, Int. J. Heat Mass Transfer 167 (2021) 120824, http://dx.doi.org/10.1016/j.ijheatmasstransfer.2020.120824, URL https://www.sciencedirect.com/science/article/pii/S0017931020337625.

[6] N. Xue, W. Du, A. Gupta, W. Shyy, A. Marie Sastry, J.R.R.A. Martins, Optimization of a single lithium-ion battery cell with a gradient-based algorithm, J. Electrochem. Soc. 160 (8) (2013) A1071–A1078, http://dx.doi.org/10.1149/2.036308jes.

[7] M. Astaneh, J. Andric, L. Löfdahl, D. Maggiolo, P. Stopp, M. Moghaddam, M. Chapuis, H. Ström, Calibration optimization methodology for lithium-ion battery pack model for electric vehicles in mining applications, Energies 13 (14) (2020) http://dx.doi.org/10.3390/en13143532.

[8] E. Hosseinzadeh, R. Genieser, D. Worwood, A. Barai, J. Marco, P. Jennings, A systematic approach for electrochemical-thermal modelling of a large format lithium-ion battery for electric vehicle application, J. Power Sources 382 (2018) 77–94, http://dx.doi.org/10.1016/j.jpowsour.2018.02.027, URL http://www.sciencedirect.com/science/article/pii/S0378775318301411.

[9] H. Lundgren, Thermal Aspects and Electrolyte Mass Transport in Lithium-ion Batteries (Ph.D. thesis), Applied Electrochemistry, Chemical Engineering and Technology, School of Chemical Science and Engineering (CHE), KTH, 2015, p. 60, http://kth.diva-portal.org/smash/get/diva2:812776/FULLTEXT01.pdf, http://urn.kb.se/resolve?urn=urn:nbn:se:kth:diva-166857.

[10] C. Heubner, K. Nikolowski, S. Reuber, M. Schneider, M. Wolter, A. Michaelis, Recent insights into rate performance limitations of Li-ion batteries, Batter. Supercaps 4 (2) (2021) 268–285, http://dx.doi.org/10.1002/batt.202000227.

[11] D.E. Eapen, R. Suresh, S. Patil, R. Rengaswamy, A systems engineering perspective on electrochemical energy technologies and a framework for application driven choice of technology, Renew. Sustain. Energy Rev. 147 (2021) 111165, http://dx.doi.org/10.1016/j.rser.2021.111165, URL https://www.sciencedirect.com/science/article/pii/S1364032121004548.

[12] V. Ramadesigan, P.W.C. Northrop, S. De, S. Santhanagopalan, R.D. Braatz, V.R. Subramanian, Modeling and simulation of lithium-ion batteries from a systems engineering perspective, J. Electrochem. Soc. 159 (3) (2012) R31 –R45.

[13] M. Xu, B. Reichman, X. Wang, Modeling the effect of electrode thickness on the performance of lithium-ion batteries with experimental validation, Energy 186 (2019) 115864, http://dx.doi.org/10.1016/j.energy.2019.115864, URL http://www.sciencedirect.com/science/article/pii/S0360544219315361.

[14] R.C. Progelhof, J.L. Throne, R.R. Ruetsch, Methods for predicting the thermal conductivity of composite systems: A review, Polymer Eng.Sci. 16 (9) (1976) 615–625, http://dx.doi.org/10.1002/pen.760160905.

[15] K.S. Reddy, P. Karthikeyan, Combinatory models for predicting the effective thermal conductivity of frozen and unfrozen food materials, Adv. Mech. Eng. 2 (2010) 901376, http://dx.doi.org/10.1155/2010/901376.

[16] I. Nozad, R.G. Carbonell, S. Whitaker, Heat conduction in multiphase systems—I: Theory and experiment for two-phase systems, Chem. Eng. Sci. 40 (5) (1985) 843–855, http://dx.doi.org/10.1016/0009-2509(85)85037-5, URL https://www.sciencedirect.com/science/article/pii/0009250985850375.

[17] W.B. Gu, C.Y. Wang, Thermal-electrochemical modeling of battery systems, J. Electrochem. Soc. 147 (8) (2000) 2910–2922, http://dx.doi.org/10.1149/1.1393625, URL http://jes.ecsdl.org/content/147/8/2910.abstract.

[18] J. Polansky, N. Jeffers, J. Punch, A hybrid approach for predicting the effective thermal conductivity of sintered porous materials, Int. J. Therm. Sci. 148 (2020) 106135, http://dx.doi.org/10.1016/j.ijthermalsci.2019.106135, URL https://www.sciencedirect.com/science/article/pii/S1290072919311627.

[19] D. Werner, A. Loges, D.J. Becker, T. Wetzel, Thermal conductivity of Li-ion batteries and their electrode configurations – A novel combination of modelling and experimental approach, J. Power Sources 364 (2017) 72–83, http://dx.doi.org/10.1016/j.jpowsour.2017.07.105, URL https://www.sciencedirect.com/science/article/pii/S037877531731011X.

[20] H. Wei, S. Zhao, Q. Rong, H. Bao, Predicting the effective thermal conductivities of composite materials and porous media by machine learning methods, Int. J. Heat Mass Transfer 127 (2018) 908–916, http://dx.doi.org/10.1016/j.ijheatmasstransfer.2018.08.082, URL https://www.sciencedirect.com/science/article/pii/S0017931018317423.

[21] L. Shen, Z. Chen, Critical review of the impact of tortuosity on diffusion, Chem. Eng. Sci. 62 (14) (2007) 3748–3755, http://dx.doi.org/10.1016/j.ces.2007.03.041, URL https://www.sciencedirect.com/science/article/pii/S0009250907003144.

[22] B. Tjaden, D.J.L. Brett, P.R. Shearing, Tortuosity in electrochemical devices: a review of calculation approaches, Int. Mater. Rev. 63 (2) (2018) 47–67, http://dx.doi.org/10.1080/09506608.2016.1249995.

[23] D.A.G. Bruggeman, Berechnung verschiedener physikalischer konstanten von heterogenen substanzen. I. Dielektrizitätskonstanten und leitfähigkeiten der mischkörper aus isotropen substanzen, Ann. Der Phys. 416 (7) (1935) 636–664, http://dx.doi.org/10.1002/andp.19354160705.

[24] B. Tjaden, S.J. Cooper, D.J.L. Brett, D. Kramer, P.R. Shearing, On the origin and application of the bruggeman correlation for analysing transport phenomena in electrochemical systems, Curr. Opin. Chem. Eng. 12 (2016) 44–51, http://dx.doi.org/10.1016/j.coche.2016.02.006, URL https://www.sciencedirect.com/science/article/pii/S2211339816300119.

[25] C. Han, Z. Chen, Study on electrochemical and mass transfer coupling characteristics of proton exchange membrane (PEM) fuel cell based on a fin-like electrode surface, Int. J. Hydrogen Energy 43 (16) (2018) 8026–8039, http://dx.doi.org/10.1016/j.ijhydene.2018.02.177, URL https://www.sciencedirect.com/science/article/pii/S0360319918306803.

[26] B. Laoun, M.W. Naceur, A. Khellaf, A.M. Kannan, Global sensitivity analysis of proton exchange membrane fuel cell model, Int. J. Hydrogen Energy 41 (22) (2016) 9521–9528, http://dx.doi.org/10.1016/j.ijhydene.2016.04.046, URL https://www.sciencedirect.com/science/article/pii/S0360319915318346.

[27] E. Hosseinzadeh, J. Marco, P. Jennings, Electrochemical-thermal modelling and optimisation of lithium-ion battery design parameters using analysis of variance, Energies 10 (9) (2017) http://dx.doi.org/10.3390/en10091278.

[28] M. Astaneh, R. Dufo-López, R. Roshandel, F. Golzar, J.L. Bernal-Agustín, A computationally efficient Li-ion electrochemical battery model for long-term analysis of stand-alone renewable energy systems, J. Energy Storage 17 (2018) 93–101, http://dx.doi.org/10.1016/j.est.2018.02.015, URL http://linkinghub.elsevier.com/retrieve/pii/S2352152X17305017.

[29] I.V. Thorat, D.E. Stephenson, N.A. Zacharias, K. Zaghib, J.N. Harb, D.R. Wheeler, Quantifying tortuosity in porous li-ion battery materials, J. Power Sources 188 (2) (2009) 592–600, http://dx.doi.org/10.1016/j.jpowsour.2008.12.032, URL http://www.sciencedirect.com/science/article/pii/S0378775308023574.

[30] M. Jabbari, R. Wang, Z. Liang, M.N. Esfahani, E. Hosseinzadeh, Numerical modelling of nanocomposite conductive plate for battery thermal management using a novel multi-domain approach, Appl. Therm. Eng. 182 (2021) 116067, http://dx.doi.org/10.1016/j.applthermaleng.2020.116067, URL https://www.sciencedirect.com/science/article/pii/S135943112033547X.

[31] A. Vadakkepatt, B. Trembacki, S.R. Mathur, J.Y. Murthy, Bruggeman's exponents for effective thermal conductivity of lithium-ion battery electrodes, J. Electrochem. Soc. 163 (2) (2015) A119–A130, http://dx.doi.org/10.1149/2.0151602jes.

[32] G.M. Goldin, A.M. Colclasure, A.H. Wiedemann, R.J. Kee, Three-dimensional particle-resolved models of Li-ion batteries to assist the evaluation of empirical parameters in one-dimensional models, Electrochim. Acta 64 (2012) 118–129, http://dx.doi.org/10.1016/j.electacta.2011.12.119, URL https://www.sciencedirect.com/science/article/pii/S0013468612000035.

[33] J. Guo, Z. Liu, B. Yang, X. Yang, J. Yan, Melting assessment on the angled fin design for a novel latent heat thermal energy storage tube, Renew. Energy 183 (2022) 406–422, http://dx.doi.org/10.1016/j.renene.2021.11.007, URL https://www.sciencedirect.com/science/article/pii/S0960148121015767.

[34] J. Guo, Z. Du, G. Liu, X. Yang, M.-J. Li, Compression effect of metal foam on melting phase change in a shell-and-tube unit, Appl. Therm. Eng. 206 (2022) 118124, http://dx.doi.org/10.1016/j.applthermaleng.2022.118124, URL https://www.sciencedirect.com/science/article/pii/S1359431122000886.

[35] X. Yang, J. Guo, B. Yang, H. Cheng, P. Wei, Y.-L. He, Design of non-uniformly distributed annular fins for a shell-and-tube thermal energy storage unit, Appl. Energy 279 (2020) 115772, http://dx.doi.org/10.1016/j.apenergy.2020.115772, URL https://www.sciencedirect.com/science/article/pii/S0306261920312587.

[36] M. Seddiq, M. Maerefat, M. Mirzaei, Modeling of heat transfer at the fluid–solid interface by lattice Boltzmann method, Int. J. Therm. Sci. 75 (2014) 28–35, http://dx.doi.org/10.1016/j.ijthermalsci.2013.07.014, URL https://www.sciencedirect.com/science/article/pii/S1290072913001713.

[37] H. Karani, C. Huber, Lattice Boltzmann formulation for conjugate heat transfer in heterogeneous media, Phys. Rev. E 91 (2) (2015) 23304, http://dx.doi.org/10.1103/PhysRevE.91.023304, URL https://link.aps.org/doi/10.1103/PhysRevE.91.023304.

[38] D. Maggiolo, F. Picano, F. Zanini, S. Carmignato, M. Guarnieri, S. Sasic, H. Ström, Solute transport and reaction in porous electrodes at high Schmidt numbers, J. Fluid Mech. 896 (2020) A13, http://dx.doi.org/10.1017/jfm.2020.344, URL https://www.cambridge.org/core/article/solute-transport-and-reaction-in-porous-electrodes-at-high-schmidt-numbers/F3E3FC376F14375475B048D1C56E5B10.

[39] H. Wang, Y. Yin, X.Y. Hui, J.Q. Bai, Z.G. Qu, Prediction of effective diffusivity of porous media using deep learning method based on sample structure information self-amplification, Energy AI 2 (2020) 100035, http://dx.doi.org/10.1016/j.egyai.2020.100035, URL https://www.sciencedirect.com/science/article/pii/S2666546820300355.

[40] L. Chen, Y.-L. Feng, C.-X. Song, L. Chen, Y.-L. He, W.-Q. Tao, Multi-scale modeling of proton exchange membrane fuel cell by coupling finite volume method and lattice Boltzmann method, Int. J. Heat Mass Transfer 63 (2013) 268–283, http://dx.doi.org/10.1016/j.ijheatmasstransfer.2013.03.048, URL https://www.sciencedirect.com/science/article/pii/S001793101300255X.

[41] G. Qiu, A.S. Joshi, C.R. Dennison, K.W. Knehr, E.C. Kumbur, Y. Sun, 3-D pore-scale resolved model for coupled species/charge/fluid transport in a vanadium redox flow battery, Electrochim. Acta 64 (2012) 46–64, http://dx.doi.org/10.1016/j.electacta.2011.12.065, URL https://www.sciencedirect.com/science/article/pii/S001346861101886X.

[42] Z.Y. Jiang, Z.G. Qu, L. Zhou, W.Q. Tao, A microscopic investigation of ion and electron transport in lithium-ion battery porous electrodes using the lattice Boltzmann method, Appl. Energy 194 (2017) 530–539, http://dx.doi.org/10.1016/j.apenergy.2016.10.125, URL https://www.sciencedirect.com/science/article/pii/S0306261916315756.

[43] Z.Y. Jiang, Z.G. Qu, L. Zhou, Lattice Boltzmann simulation of ion and electron transport during the discharge process in a randomly reconstructed porous electrode of a lithium-ion battery, Int. J. Heat Mass Transfer 123 (2018) 500–513, http://dx.doi.org/10.1016/j.ijheatmasstransfer.2018.03.004, URL https://www.sciencedirect.com/science/article/pii/S0017931017330831.

[44] S.W. Peterson, The Effect of Microstructure On Transport Properties of Porous Electrodes (Ph.D. thesis), Brigham Young University, 2015, URL https://scholarsarchive.byu.edu/cgi/viewcontent.cgi?article=5430{&}context=etd.

[45] D. Oehler, P. Seegert, T. Wetzel, Modeling the thermal conductivity of porous electrodes of Li-ion batteries as a function of microstructure parameters, Energy Technol. 9 (6) (2021) 2000574, http://dx.doi.org/10.1002/ente.202000574.

[46] M. Ioannidis, M. Kwiecien, I. Chatzis, Statistical analysis of the porous microstructure as a method for estimating reservoir permeability, J. Pet. Sci. Eng. 16 (1996) 251–261.

[47] K.K. Bodla, S.V. Garimella, J.Y. Murthy, 3D reconstruction and design of porous media from thin sections, Int. J. Heat Mass Transfer 73 (2014) 250–264, http://dx.doi.org/10.1016/j.ijheatmasstransfer.2014.02.006, URL https://www.sciencedirect.com/science/article/pii/S0017931014001239.

[48] W.K. Epting, S. Litster, Effects of an agglomerate size distribution on the PEFC agglomerate model, Int. J. Hydrogen Energy 37 (10) (2012) 8505–8511, http://dx.doi.org/10.1016/j.ijhydene.2012.02.099, URL https://www.sciencedirect.com/science/article/pii/S0360319912004636.

[49] D. Zhang, A. Forner-Cuenca, O.O. Taiwo, V. Yufit, F.R. Brushett, N.P. Brandon, S. Gu, Q. Cai, Understanding the role of the porous electrode microstructure in redox flow battery performance using an experimentally validated 3D pore-scale lattice Boltzmann model, J. Power Sources 447 (2020) 227249, http://dx.doi.org/10.1016/j.jpowsour.2019.227249, URL https://www.sciencedirect.com/science/article/pii/S037877531931242X.

[50] J. Ramousse, J. Deseure, O. Lottin, S. Didierjean, D. Maillet, Modelling of heat, mass and charge transfer in a PEMFC single cell, J. Power Sources 145 (2) (2005) 416–427, http://dx.doi.org/10.1016/j.jpowsour.2005.01.067, URL https://www.sciencedirect.com/science/article/pii/S0378775305002910.

[51] J.J. Hwang, P.Y. Chen, Heat/mass transfer in porous electrodes of fuel cells, Int. J. Heat Mass Transfer 49 (13) (2006) 2315–2327, http://dx.doi.org/10.1016/j.ijheatmasstransfer.2005.11.021, URL https://www.sciencedirect.com/science/article/pii/S0017931006000056.

[52] J.H. Lu, H.Y. Lei, C.S. Dai, A lattice Boltzmann algorithm for simulating conjugate heat transfer through virtual heat capacity correction, Int. J. Therm. Sci. 116 (2017) 22–31, http://dx.doi.org/10.1016/j.ijthermalsci.2017.02.006, URL https://www.sciencedirect.com/science/article/pii/S1290072916311450.

[53] P.L. Bhatnagar, E.P. Gross, M. Krook, A model for collision processes in gases. I. Small amplitude processes in charged and neutral one-component systems, Phys. Rev. 94 (3) (1954) 511–525, http://dx.doi.org/10.1103/PhysRev.94.511, URL https://link.aps.org/doi/10.1103/PhysRev.94.511.

[54] L.F. Arenas, C. Ponce de León, F.C. Walsh, Redox flow batteries for energy storage: their promise, achievements and challenges, Curr. Opin. Electrochem. 16 (2019) 117–126, http://dx.doi.org/10.1016/j.coelec.2019.05.007, URL https://www.sciencedirect.com/science/article/pii/S2451910319300183.

[55] S. He, B.T. Habte, F. Jiang, LBM prediction of effective electric and species transport properties of lithium-ion battery graphite anode, Solid State Ion. 296 (2016) 146–153, http://dx.doi.org/10.1016/j.ssi.2016.09.021, URL https://www.sciencedirect.com/science/article/pii/S0167273816306208.

[56] U.S. Kim, C.B. Shin, C.-S. Kim, Modeling for the scale-up of a lithium-ion polymer battery, J. Power Sources 189 (1) (2009) 841–846, http://dx.doi.org/10.1016/j.jpowsour.2008.10.019, URL https://www.sciencedirect.com/science/article/pii/S0378775308019149.

[57] R. Kantharaj, A.M. Marconnet, Heat generation and thermal transport in lithium-ion batteries: A scale-bridging perspective, Nanoscale Microscale Thermophys. Eng. 23 (2) (2019) 128–156, http://dx.doi.org/10.1080/15567265.2019.1572679.

[58] G. Karimi, X. Li, Thermal management of lithium-ion batteries for electric vehicles, Int. J. Energy Res. 37 (1) (2013) 13–24, http://dx.doi.org/10.1002/er.1956.

[59] Z. Koza, M. Matyka, A. Khalili, Finite-size anisotropy in statistically uniform porous media, Phys. Rev. E 79 (6) (2009) 66306, http://dx.doi.org/10.1103/PhysRevE.79.066306, URL https://link.aps.org/doi/10.1103/PhysRevE.79.066306.

[60] J.P. Angle, Z. Wang, C. Dames, M.L. Mecartney, Comparison of two-phase thermal conductivity models with experiments on dilute ceramic composites, J. Am. Ceram. Soc. 96 (9) (2013) 2935–2942, http://dx.doi.org/10.1111/jace.12488.

[61] L. Wei, Z. Lu, F. Cao, L. Zhang, X. Yang, X. Yu, L. Jin, A comprehensive study on thermal conductivity of the lithium-ion battery, Int. J. Energy Res. 44 (12) (2020) 9466–9478, http://dx.doi.org/10.1002/er.5016.

[62] A. Duda, Z. Koza, M. Matyka, Hydraulic tortuosity in arbitrary porous media flow, Phys. Rev. E 84 (3) (2011) 36319, http://dx.doi.org/10.1103/PhysRevE.84.036319, URL https://link.aps.org/doi/10.1103/PhysRevE.84.036319.

[63] C. Liu, L. Liu, Optimal design of li-ion batteries through multi-physics modeling and multi-objective optimization, J. Electrochem. Soc. 164 (11) (2017) E3254–E3264, http://dx.doi.org/10.1149/2.0291711jes.

[64] SNIC, Swedish National infrastrucutre for computing, 2020, URL https://www.snic.se/.